Photonics-based Broadband MIMO Radar with Segmented Digital Beamforming Enabling Beam Squint-Free Fast Imaging

Jiayuan Kong, Fangzheng Zhang, *Senior member, IEEE*, Guanqun Sun, Yuewen Zhou, Jinhu Li, Yihan Wang, Yuhui He and Shilong Pan, *Fellow, IEEE*

***Abstract*—Photonics-based broadband multi-input multi-output (MIMO) radar is a promising solution for high-resolution 2D imaging. While the ultra-wide bandwidth enables centimeter-level range resolution, it fundamentally conflicts with conventional narrowband beamforming, introducing severe beam squint and degrading angular accuracy. Although scanning time delay (STD)-compensated digital beamforming (DBF) can mitigate this issue, its point-by-point phase compensation imposes a computational burden, hindering real-time applications. To resolve this problem, this paper proposes a computationally efficient segmented DBF algorithm. Leveraging the time-frequency mapping property of photonics-based de-chirped signals, the proposed algorithm divides the time-domain echo into sub-segments equivalent to frequency sub-bands. This allows for parallel narrowband processing that effectively eliminates beam squint and suppresses grating lobes without the heavy computational cost of STD compensation. The system is experimentally validated using a 2×4 photonics-based MIMO radar with an 8 GHz bandwidth. Results demonstrate a range resolution of 2.04 cm and an angular resolution of 1.0°. Notably, the proposed algorithm achieves an imaging speed 7.1 times faster than the STD-compensated DBF algorithm while maintaining comparable imaging quality.**

***Index Terms*—photonics-based broadband radar, multi-input multi-output (MIMO), digital beamforming (DBF), beam squint, fast imaging.**

I. INTRODUCTION

Radar systems play a crucial role in modern military and civilian applications [1]–[5]. With the increasing deployment of clustered targets in recent years, radar systems are required to discriminate multiple closely spaced targets [6]. Conventional radar systems, however, often struggle with this task due to their inherent resolution limitations [7], [8]. Recently, photonics-based radar systems [9]–[14] have emerged as a promising solution, demonstrating exceptional performance in achieving high range resolution. For instance, one implementation [12] leverages photonic frequency quadrupling and de-chirping techniques for broadband signal generation and processing, achieving a centimeter-level range resolution of 1.875 cm.

To extend this high resolution to the 2D spatial domain, many photonics-based systems rely on the inverse synthetic aperture radar (ISAR) principle [13], [15]. Although ISAR can provide high-resolution 2D imaging, it relies on target motion to synthesize the aperture, limiting its applicability to static or slowly moving scenes. To enable imaging independent of target motion, array architectures are required [16], [17]. In particular, multi-input multi-output (MIMO) arrays have garnered significant interest, as they synthesize a large virtual aperture using a reduced number of physical antennas, thereby optimizing system cost and complexity [18]. The integration of MIMO array principles with photonics-based broadband radar thus presents a compelling route to achieve high-resolution 2D imaging simultaneously in both the range and angular domains [19]. For clustered small-target scenarios, improved range and angular resolutions enable the radar to distinguish closely spaced targets more effectively. Meanwhile, fast 2D imaging is essential for real-time detection, motivating a broadband MIMO imaging method that combines high resolution with high computational efficiency. However, as the operating bandwidth of photonics-based radar expands, the narrowband assumption in conventional beamforming models becomes invalid. Consequently, the direct application of narrowband beamforming to broadband signals results in beam squint and a significant degradation of imaging performance [20], [21].

To mitigate beam squint, various approaches have been explored. In the analog domain, optical true-time delay (TTD) techniques, including fiber grating delay lines and integrated optical TTD modules, offer a potential solution to mitigate beam squint [22]–[24]. However, TTD implementations often suffer from high complexity, cost, and limited stability. Therefore, digital compensation algorithms have emerged as flexible and reconfigurable alternatives. They eliminate the need for physical delay lines and facilitate fully digital beamforming (DBF) [25], [26]. A common approach involves

This work was supported in part by the National Natural Science Foundation of China under Grant (No. 62371224), in part by the Shanghai Aerospace Science and Technology Innovation Foundation (SAST2024-023), in part by the Open Found of IPOC (BUPT), in part by the Aviation Science Foundation of China under Grant 2015ZC52024, and in part by the Key Laboratory of Radar Imaging and Microwave Photonics (NUAA), Ministry of Education, under Grant NJ20250001. (*Corresponding author: Fangzheng Zhang; Guanqun Sun*)

Jiayuan Kong, Fangzheng Zhang, Yuewen Zhou, Jinhu Li, YihanWang, Yuhui He and Shilong Pan are with the National Key Laboratory of Microwave Photonics, Nanjing University of Aeronautics and Astronautics, Nanjing 210016, China.

Guanqun Sun is with the School of Computer and Electronic Information, Nanjing Normal University, Nanjing 210023, China.

Color versions of one or more of the figures in this article are available online at http://ieeexplore.ieee.org transforming the received echoes into the frequency domain via an FFT, performing beamforming there, and then applying an IFFT to recover the time-domain signal. While effective for directly sampled broadband radars, these frequency-domain methods are generally unsuitable for the de-chirped architectures prevalent in microwave photonic array radars. To address this gap, the scanning time delay (STD)-compensated DBF algorithm was proposed for de-chirp-based microwave photonic array radars [27]. By performing point-by-point phase compensation in the de-chirped domain, this algorithm ensures consistent steering vectors across the bandwidth, effectively eliminating beam squint. Nevertheless, its computational burden increases with the number of array elements and fast-time samples. This scaling poses a major bottleneck for real-time imaging applications, especially in broadband MIMO radar systems with large virtual apertures.

In this work, a microwave photonic broadband MIMO radar system [28] is implemented and experimentally demonstrated. This system integrates photonic frequency quadrupling for broadband signal generation and photonic frequency de-chirping for efficient signal processing. Building upon this high-resolution architecture, we propose a segmented DBF algorithm tailored to enable fast, beam squint-free 2D imaging. The proposed method exploits the time-frequency mapping property of de-chirped linear frequency modulated (LFM) signals. By dividing the broadband signal into multiple sub-segments in the time domain, the algorithm effectively partitions the signal into narrowband sub-bands. This segmentation enables accurate squint correction and allows for parallel processing, drastically reducing computational complexity. Experimental evaluations are performed using a 2×4 microwave photonic MIMO radar with an 8 GHz bandwidth per channel. Experimental results in both single and multiple unmanned aerial vehicle (UAV) detection scenarios demonstrate that the system achieves range and angular resolutions of 2.04 cm and 1.0°, respectively. Furthermore, the segmented DBF algorithm is shown to effectively correct beam squint and suppress grating lobes, achieving an imaging speed 7.1 times faster than the STD-compensated DBF algorithm.

II. System Architecture and Principle

A. System Architecture

The architecture of the implemented microwave photonic broadband time-division multiplexing (TDM) MIMO radar is illustrated in Fig. 1. The system comprises three main functional blocks: a photonic transmitter, a photonic receiver, and a synchronization unit and control unit. In the transmitter, a continuous wave (CW) optical carrier from a laser diode (LD) is modulated by a dual-parallel Mach-Zehnder modulator (DPMZM). Driven by a pair of orthogonal intermediate-frequency linear frequency modulated (IF-LFM) signals (generated by an electrical signal generator, ESG), the DPMZM is biased to suppress the carrier and generate ±2nd-order modulation sidebands. Here, the ±2nd -order sidebands are selected because their beating at the photodetector produces a frequency-quadrupled RF-LFM signal, thereby enabling broadband microwave signal generation from a lower-frequency electrical drive. This optical signal is amplified by an erbium-doped fiber amplifier (EDFA) and split into N+1 paths. One path feeds the transmission link, while the other N paths serve as optical reference signals for the coherent receivers.

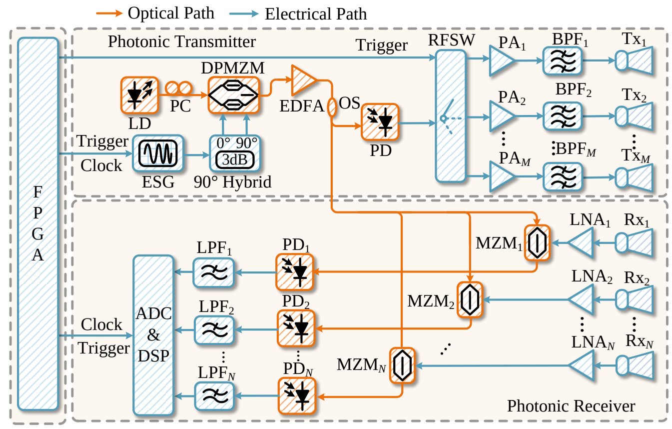

Fig. 1. The system architecture of the microwave photonic broadband TDM-MIMO radar.

For transmission, the optical signal is converted to an electrical microwave signal via a high-speed photodetector (PD). A high-isolation RF switch (RFSW), synchronized with the radar pulse repetition interval (PRI), sequentially routes the signal to M transmit antennas in a time-division multiplexing (TDM) manner. This TDM scheme ensures orthogonality between channels, simplifying the hardware by eliminating the need for multiple simultaneous transmitters. Each transmit signal is then amplified by a power amplifier (PA) and filtered by a band-pass filter (BPF) to filter the frequency-quadrupled component prior to radiation. The radiated signal in the m^{th} channel, after frequency quadrupling, has an instantaneous frequency of $f = 4f_0+4kt$ ($0 \le t \le T_w$), expressed as

$$S_{tx}(t,m) = \mathrm{rect}\left\{\frac{t-T_w/2-(m-1)T_p}{T_w}\right\} \cdot \cos\left\{2\pi\left(4f_0+2k\left(t-(m-1)T_p\right)\right)\left(t-(m-1)T_p\right)\right\} \tag{1}$$

where f_0, k, T_w, and T_p denote the starting frequency, chirp rate, pulse width, and pulse repetition period, respectively. The photonic frequency quadrupling technique enables efficient broadband signal generation, overcoming the bandwidth limitations inherent in electric methods.

In the receiver, echoes captured by N antennas are amplified and fed into N individual Mach-Zehnder modulators (MZMs). These modulators mix the received RF echoes with the optical reference signals for photonic frequency de-chirping. Finally, for each of the M transmitted waveforms, a total of $M\times N$ de-chirped signals are acquired. The de-chirped signals from the mn^{th} ($1 \le mn \le MN$) channel can be expressed as

$$S_{de}(t,m,n) = \mathrm{rect}\left\{\frac{t-T_w/2-(m-1)T_p-\tau(m,n)}{T_w-\tau(m,n)}\right\} \cdot \cos\left\{\begin{array}{l} 8\pi k\tau(m,n)\cdot\left(t-(m-1)T_p\right) \\ +8\pi f_0\tau(m,n)-4\pi k\tau^2(m,n) \end{array}\right\} \tag{2}$$

This article has been accepted for publication in Journal of Lightwave Technology. This is the author's version which has not been fully edited and content may change prior to final publication. Citation information: DOI 10.1109/JLT.2026.3703868

where $\tau(m,n)$ denotes the propagation delay of the path from the m^{th} transmit antenna to the n^{th} receive antenna via the target reflection. The de-chirped outputs from all N receive channels are digitized in parallel by N analog-to-digital converters (ADCs) and transferred to the digital signal processing (DSP) unit for subsequent analysis. Since the ADCs sample the de-chirped beat signals rather than the original broadband echoes, the required sampling rate is determined by the maximum beat frequency within the target detection range instead of the transmitted signal bandwidth. Thus, photonic frequency de-chirping compresses the broadband echoes into the IF domain, significantly reducing the ADC sampling requirements. Meanwhile, the MIMO configuration enlarges the virtual aperture without adding physical antennas, thereby enhancing angular resolution.

In the synchronization and control unit, a field-programmable gate array (FPGA) supplies a common reference clock and a trigger to the ESG, ADCs, and the RFSW to guarantee synchronization. The reference clock synchronizes the frequency sources in the ESG and ADCs. Simultaneously, the trigger signal aligns the timing of radar pulse transmission (via the ESG and RFSW) and echo acquisition (via the ADCs).

B. Signal Model of TDM-MIMO Array

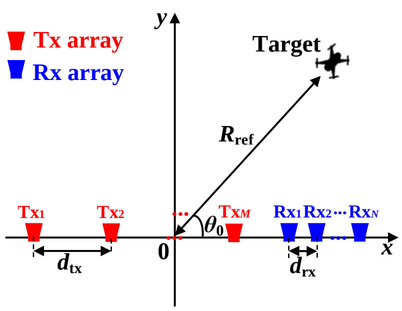

Fig. 2. The geometric configuration of a TDM-MIMO radar system.

As illustrated in Fig. 2, the TDM-MIMO radar employs a linear transmit array and a linear receive array, with adjacent Tx and Rx element spacings denoted by d_{tx} and d_{rx}, respectively. A far-field point target is located at a reference range R_{ref} and an angle θ_0 with respect to the array broadside. Under the far-field assumption, the physical Tx-Rx array synthesizes an equivalent virtual array with MN elements [29]. Due to the TDM operation of the transmitter, echoes from different transmit antennas occupy distinct, non-overlapping time slots within each PRI. After serial-to-parallel conversion of the TDM data, the de-chirped signal for the mn-th virtual channel, corresponding to the m-th Tx and n-th Rx, can be modeled as

$$S'_{\text{de}}(t,mn)=\text{rect}\left\{\frac{t-T_{\text{w}}/2-\tau(m,n)}{T_{\text{w}}-\tau(m,n)}\right\}\cdot\cos\left\{\begin{aligned}&8\pi k\tau(m,n)t+8\pi f_0\tau(m,n)\\&-4\pi k\tau^2(m,n)\end{aligned}\right\} \tag{3}$$

where the compact expression serves as the basis for subsequent range and angle processing. In Eq. (4), the key parameter $\tau(m,n)$, is determined by the spatial configuration of the array.

According to the geometry in Fig. 2, the two-way propagation delay for the mn^{th} virtual channel is given by

$$\begin{aligned}\tau(m,n)&=\frac{2\left(R_{\text{ref}}-d(m,n)\sin(\theta_0)\right)}{c}\\ d(m,n)&=\frac{1}{2}\left((m-1)d_{\text{tx}}+(n-1)d_{\text{rx}}\right)\end{aligned} \tag{4}$$

where $d(m,n)$ is the spatial distance between the mn^{th} virtual element and the first virtual element. By further substituting (4) into (3), the de-chirped signal for the mn^{th} virtual element can be further written as

$$\begin{aligned}S'_{\text{de}}(t,mn)&=\text{rect}(t,m,n)\cdot\cos\left\{\begin{aligned}&\varphi(t)+\psi(t,m,n)\\&+\xi+\chi(m,n)\end{aligned}\right\}\\ \text{rect}(t,m,n)&=\text{rect}\left\{\frac{t-T_{\text{w}}/2-\left(2R_{\text{ref}}-2d(m,n)\sin(\theta_0)\right)/c}{T_{\text{w}}-\left(2R_{\text{ref}}-2d(m,n)\sin(\theta_0)\right)/c}\right\}\\ \varphi(t)&=8\pi k\frac{2R_{\text{ref}}}{c}t\\ \psi(t,m,n)&=8\pi\left(-f_0-kt+k\frac{2R_{\text{ref}}}{c}\right)\frac{2d(m,n)\sin(\theta_0)}{c}\\ \xi&=8\pi f_0\frac{2R_{\text{ref}}}{c}\\ \chi(m,n)&=-4\pi k\left(\frac{2R_{\text{ref}}}{c}\right)^2-4\pi k\left(\frac{2d(m,n)\sin(\theta_0)}{c}\right)^2\end{aligned} \tag{5}$$

where the rectangular function rect(t,m,n) has an effective pulse width of $T_{\text{w}}-(2R_{\text{ref}}-2d(m,n)\sin(\theta_0))/c$. The phase term $\varphi(t)$ contains the range information R_{ref}, which can be extracted in the time domain via fast-time FFT. The phase term $\psi(t,m,n)$ corresponds to the angle information θ_0, which can be extracted in the virtual array domain through array signal processing. And the phase term ξ represents a fixed phase shift independent of time or array information. The residual term $\chi(m,n)$ is relatively small compared with the other phase terms and can thus be neglected. Thus, the de-chirped signal is approximated as

$$S'_{\text{de}}(t,mn)\approx\text{rect}(t,m,n)\cdot\cos\left\{\varphi(t)+\psi(t,m,n)+\xi\right\} \tag{6}$$

Assuming an ADC sampling rate of f_{s}, with a corresponding sampling interval $T_{\text{s}}=1/f_{\text{s}}$, the MN de-chirped signals are digitized into MN discrete-time data. For each channel, the number of sampling points within a pulse width is $L=T_{\text{w}}/T_{\text{s}}$. The sampled signal of the mn^{th} virtual channel can be written as

$$S'_{\text{de}}(t,mn)\xrightarrow{\text{ADC}}S'_{\text{de}}[l,mn],1\le l\le L \tag{7}$$

where l is the fast-time sample index. These digitized de-chirped data form the input for the subsequent broadband array signal processing. For narrowband signals, conventional digital beamforming (DBF) can be directly applied to extract angular information. However, when processing broadband signals, conventional DBF suffers from beam squint, which severely degrades the quality and accuracy of the 2D imaging result.

To address the beam squint problem, a STD-compensated DBF [27] algorithm was proposed for broadband array radar systems. This algorithm compensates for the beam squint effect by applying a phase correction term, $-8\pi k\Delta\tau(m,n,\theta_q)t$, to the received signals.

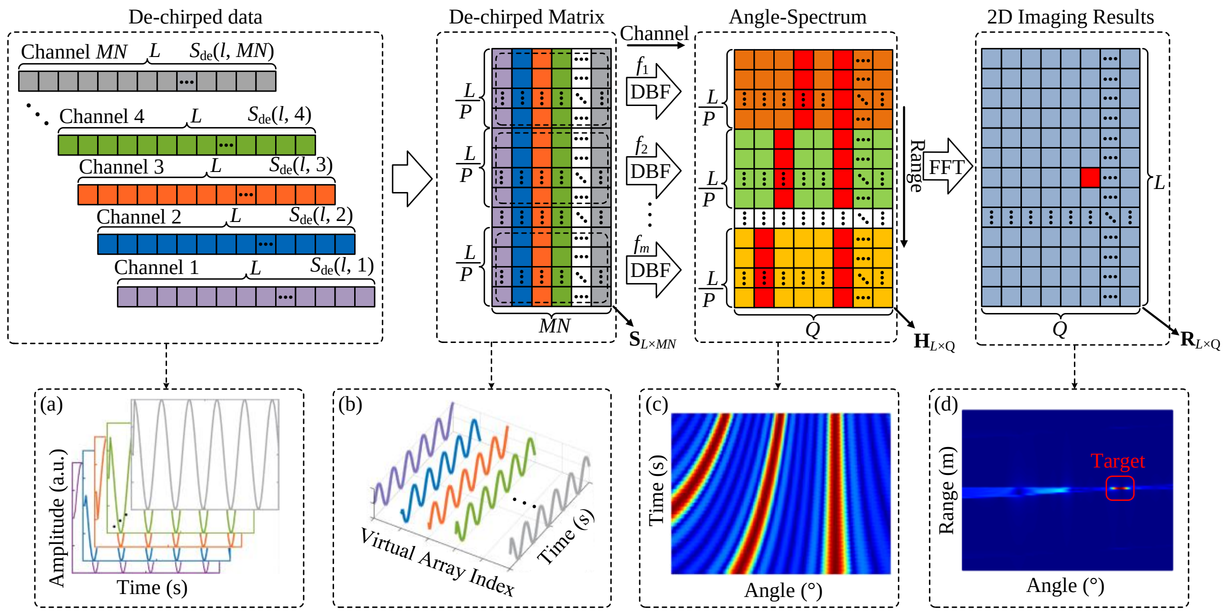

Fig. 3. The signal processing flow of broadband array radar with segmented DBF for 2D imaging. (a) De-chirped data from *MN* virtual channels. (b) De-chirped matrix after fast-time segmentation. (c) Angle spectrum after segmented DBF. (d) Final 2D imaging results. The imaging results are generated from simulated single-point-target data for illustration.

This algorithm compensates for the beam squint effect by applying a phase correction term, $-8\pi k\Delta\tau(m,n,\theta_q)t$, to the received signals. This compensation ensures phase alignment across all virtual channels with respect to a reference channel, effectively synthesizing a time-delay response in the digital domain. For accurate imaging under far-field conditions, the exact expression of the aperture fill time $\Delta\tau(m,n,\theta_q)$ is given as

$$\Delta\tau\left(m,n,\theta_q\right)=\frac{2d\left(m,n\right)\sin\left(\theta_q\right)}{c} \tag{8}$$

where θ_q denotes the scan angle at the q^{th} scan angle. Thus, the accurately compensated signal matrix $S'_{\text{com}}(t,mn)$ can be written as

$$S'_{\text{com}}\left(t,mn\right)=S'_{\text{de}}\left(t,mn\right)\cdot\cos\left(8\pi k\Delta\tau\left(m,n\right)t\right) \tag{9}$$

After compensation, broadband DBF can be performed as

$$\mathbf{R}'_{L\times Q}=\text{FFT}\left\{S'_{\text{com}}\left(t,mn\right)\right\}\cdot\mathbf{A}'_{MN\times Q} \tag{10}$$

where FFT{·} denotes the fast-time FFT, and $\mathbf{A}'_{MN\times Q}$ is the steering vector matrix given by

$$\mathbf{A}'_{MN\times Q}=\begin{bmatrix} e^{j\phi'(1,\theta_1)} & e^{j\phi'(1,\theta_2)} & \cdots & e^{j\phi'(1,\theta_Q)} \\ e^{j\phi'(2,\theta_1)} & e^{j\phi'(2,\theta_2)} & \cdots & e^{j\phi'(2,\theta_Q)} \\ \vdots & \vdots & \ddots & \vdots \\ e^{j\phi'(MN,\theta_1)} & e^{j\phi'(MN,\theta_2)} & \cdots & e^{j\phi'(MN,\theta_Q)} \end{bmatrix} \tag{11}$$

$$\phi'(mn,\theta_q)=8\pi f_0\Delta\tau\left(m,n,\theta_q\right)$$

The STD-compensated DBF algorithm provides a robust solution for mitigating beam squint and the associated beam broadening, thereby enabling precise imaging in broadband array radar systems. To establish a theoretical performance benchmark for the implemented system, its fundamental range and angular resolutions are derived. The theoretical range resolution, a direct consequence of the transmitted bandwidth, is given by

$$r_{\text{res}}=\frac{c}{2\times B} \tag{12}$$

where c denotes the speed of light and B is the signal bandwidth [30]. Similarly, the theoretical angular resolution, enabled by the synthesized virtual aperture of the MIMO array, is expressed as

$$\theta_{\text{res}}=\frac{1}{\cos\left(\theta_{\text{tar}}\right)}\times\frac{0.886\times\lambda_c}{D} \tag{13}$$

where θ_{tar} is the target angle, λ_c is the wavelength corresponding to the highest operating frequency, and D is the virtual array aperture [31]. While the STD-compensated DBF effectively eliminates beam squint and enables high-resolution imaging, it comes at a high computational cost. As indicated in [27], the compensation operation must be repeated for every time sample L and every scanning direction Q. For high-resolution imaging requiring large L and Q, this computational burden becomes a significant bottleneck for real-time applications.

C. Segmented DBF Algorithm for 2D Imaging

To address the computational inefficiency of the STD method while maintaining squint-free performance, we propose the Segmented DBF algorithm. This approach leverages the intrinsic time-frequency mapping property of the de-chirped LFM signal.

The phase shift is reflected in the phase term $\psi(t,m,n)$ in equation (7), which contains the component $-f_0-kt+k\times2R_{\text{ref}}/c$. Given that the modulation slope k is small, the term $k\times2R_{\text{ref}}/c$ is negligible compared to f_0 and can be omitted. Under this approximation, the phase term $\psi(t,m,n)$ simplifies to

$$\psi\left(t,m,n\right)\approx-2\pi k\left(4f_0+4kt\right)\frac{2d\left(m,n\right)\sin\left(\theta_0\right)}{c} \tag{14}$$

where the phase term $\psi(t,m,n)$ varies linearly with the instantaneous frequency $4f_0+4kt$. In broadband systems, this frequency-dependent nature of the phase shift across the large signal bandwidth is the fundamental cause of beam squint. Consequently, conventional narrowband DBF, which assumes a single frequency, becomes inadequate and leads to severe performance degradation. Although an STD-compensated DBF [27] can remove the beam squint by point-by-point correction, it is computationally heavy and unfavorable for real-time operation. To simultaneously achieve squint-free imaging and high computational efficiency, we propose a segmented DBF algorithm.

As shown in Fig. 3 (a), the proposed segmented DBF algorithm begins by acquiring de-chirped data from MN virtual channels. Each virtual channel includes a time-domain sequence $S'_{\text{de}}[l,mn]$ of length L. These data are then reorganized into a de-chirped data matrix, $\boldsymbol{S}_{L\times MN}$, where each column represents a virtual channel and each row a specific fast-time sample

$$\mathbf{S}_{L\times MN}=\begin{bmatrix} S'_{\text{de}}[1,1] & S'_{\text{de}}[1,2] & \cdots & S'_{\text{de}}[1,MN] \\ S'_{\text{de}}[2,1] & S'_{\text{de}}[2,2] & \cdots & S'_{\text{de}}[2,MN] \\ \vdots & \vdots & \ddots & \vdots \\ S'_{\text{de}}[L,1] & S'_{\text{de}}[L,2] & \cdots & S'_{\text{de}}[L,MN] \end{bmatrix} = \left[s(l,1),s(l,2),\cdots,s(l,MN)\right]^{\mathrm{T}} \tag{15}$$

where $[\cdot]^{\mathrm{T}}$ denotes the transpose operation. As illustrated in the accompanying 3D plot, the data exhibits amplitude variations across both the time and virtual channel dimensions.

Then, as shown in Fig. 3 (b), the de-chirped matrix $\boldsymbol{S}_{L\times MN}$ is partitioned into P equal fast-time segments. Here, each segment contains L/P samples, where the number of samples L/P is required to be an integer. The p^{th} segment is indexed by p = 1,2, …, P and denoted as $\mathbf{X}_{(L/P)\times MN}(p)$. Each segment $\mathbf{X}_{(L/P)\times MN}(p)$ is independently processed using conventional DBF. This generates an angle-spectrum submatrix $\mathbf{H}_{(L/P)\times Q}(p)$ for Q scan angles. The segmented DBF operation can be expressed as

$$\mathbf{H}_{\frac{L}{P}\times Q}(p)=\text{DBF}\left\{\mathbf{X}_{\frac{L}{P}\times MN}(p)\right\}=\mathbf{X}_{\frac{L}{P}\times MN}(p)\times\mathbf{A}_{MN\times Q}(p) \tag{16}$$

where DBF{·} denotes the DBF operation applied to the p^{th} segment $\mathbf{X}_{(L/P)\times MN}(p)$ at its center frequency f_p. And the matrix $\mathbf{A}_{MN\times Q}(p)$ represents the steering vector corresponding to Q angular scan points and can be expressed as

$$\mathbf{A}_{MN\times Q}(p)=\begin{bmatrix} e^{j\phi_p(1,\theta_1)} & e^{j\phi_p(1,\theta_2)} & \cdots & e^{j\phi_p(1,\theta_Q)} \\ e^{j\phi_p(2,\theta_1)} & e^{j\phi_p(2,\theta_2)} & \cdots & e^{j\phi_p(2,\theta_Q)} \\ \vdots & \vdots & \ddots & \vdots \\ e^{j\phi_p(MN,\theta_1)} & e^{j\phi_p(MN,\theta_2)} & \cdots & e^{j\phi_p(MN,\theta_Q)} \end{bmatrix} \tag{17}$$

where $\phi_p(mn,\theta_q)$ denotes the phase shift associated with the mn^{th} virtual channel and the q^{th} scan angle in the p^{th} segment. Here, θ_q represents the scan angle at the q^{th} scan point used in the DBF processing, with q = 1,2, …, Q. For the implemented microwave photonic MIMO radar system in this work, the phase $\phi_p(mn, \theta_q)$ can be further expressed as

$$\begin{aligned} \phi_p(mn,\theta_q) &= 8\pi f_p\frac{2d(m,n)\sin(\theta_q)}{c} \\ f_p &= 4f_0+\frac{1}{2}\times\frac{B}{P}+p\frac{B}{P} \end{aligned} \tag{18}$$

where f_p is the center frequency of the p^{th} segment. To ensure the applicability of narrowband DBF processing within each segment, the sub-bandwidth B/P must satisfy the narrow condition. A common definition of narrowband signals is that if the bandwidth B divided by the starting frequency f_0 is less than or equal to 10%, the signal can be classified as narrowband [32], [33]. Accordingly, segmented DBF must satisfy

$$\text{s.t. } \frac{B/P}{f_0}\le 10\% \tag{19}$$

After processing all P segments, the full angle-spectrum $\mathbf{H}_{L\times Q}$ is obtained by concatenating the sub-matrices along the fast-time dimension. As shown in Fig. 3 (c), the resulting 2D plot illustrates the energy distribution across the fast-time and angle dimensions, demonstrating how the segmented DBF reconstructs the complete angle-time response. The angle-spectrum $\mathbf{H}_{L\times Q}$ can be expressed as

$$\mathbf{H}_{L\times Q}=\left[\mathbf{H}_{\frac{L}{P}\times Q}(0),\mathbf{H}_{\frac{L}{P}\times Q}(1),\cdots,\mathbf{H}_{\frac{L}{P}\times Q}(P-1)\right]^{\mathrm{T}} \tag{20}$$

Finally, as shown in Fig. 3 (d), high-resolution 2D imaging is achieved by applying a 1-D FFT along the range dimension of the angle-spectrum matrix $\mathbf{H}_{L\times Q}$, yielding the final 2D imaging result $\mathbf{R}_{L\times Q}$

$$\mathbf{R}_{L\times Q}=\text{FFT}\left\{\mathbf{H}_{L\times Q}\right\} \tag{21}$$

The corresponding range-angle map clearly demonstrates that the proposed algorithm achieves beam-squint-free and high-resolution 2D imaging.

It is worth emphasizing that this segmentation strategy can be regarded as a time-domain equivalent of channelization enabled by the time-frequency mapping of the de-chirped signal. Unlike conventional channelized radar receivers that divide a broadband signal in the frequency domain, the proposed method partitions the de-chirped IF signal directly in the fast-time domain. This avoids additional frequency-domain channelization hardware and relaxes the ADC sampling requirement while mitigating beam squint. The proposed method can also be extended to other waveforms with known time-frequency relationships, such as triangular LFM and stepped-frequency waveforms, by adapting the steering vector to the center frequency of each segment. This approach yields three significant advantages over prior arts. First, by adapting the steering vector frequency for each segment, the algorithm inherently compensates for the phase errors across the wide bandwidth, effectively eliminating beam squint. Second, the division into shorter segments drastically reduces the matrix dimensions for beamforming and facilitates parallel processing, thereby achieving a substantial acceleration in imaging speed compared to the pixel-by-pixel STD compensation. Third, the method provides inherent grating lobe suppression. In a broadband sparse array, the apparent angular location of grating lobes is varied with frequency. Since each sub-band is processed at its own center frequency, only the energy from the true target (main lobe) aligns coherently across all sub-bands after DBF and fast-time FFT, constructively integrating into a sharp peak. In contrast, the energy from grating lobes fails to align coherently,

This article has been accepted for publication in Journal of Lightwave Technology. This is the author's version which has not been fully edited and content may change prior to final publication. Citation information: DOI 10.1109/JLT.2026.3703868

becoming smeared across multiple range-angle cells in the final image and thus being significantly attenuated.

III. Experiment Demonstration

In this section, an experiment is carried out to evaluate the performance of the implemented microwave photonic MIMO radar system. The analysis is structured as follows: Section III-A details the experimental setup. Section III-B provides a comparative analysis of imaging results obtained with different DBF algorithms. Section III-C assesses the achieved range and angular resolutions. Section III-D demonstrates the multi-target detection capability. Finally, section III-E evaluates computational efficiency.

A. Experimental Setup

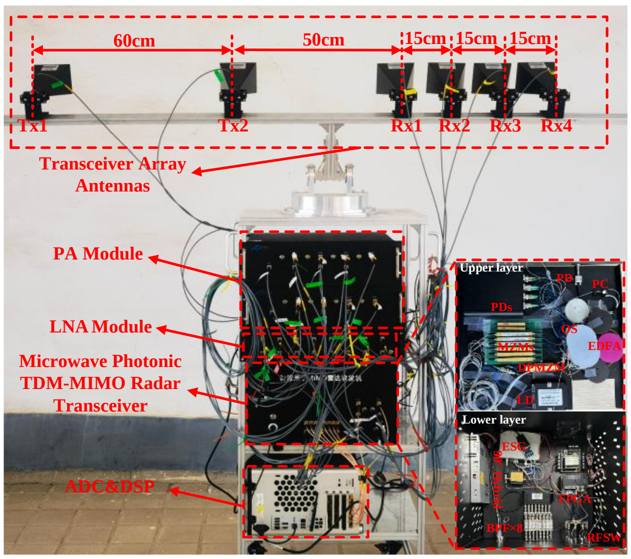

Fig. 4. The system setup of the microwave photonic broadband TDM-MIMO radar.

The experimental setup of the microwave photonic broadband TDM-MIMO radar is illustrated in Fig. 4. The transceiver array antennas (MT-BDHA1018, 20 dBi gain), the PA module (Talent Microwave TLPA1G18G-40-33, 40 dB gain and 33 dBm P1dB), the LNA module (AT-LNA-0618-5515X, 55 dB gain and 16 dBm P1dB), the ADC (Spectrum M2p.5943-x4), and the DSP together constitute the implementation of the photonic transmitter and photonic receiver. The microwave photonic TDM-MIMO radar internally incorporates the synchronization and control unit, which provides timing and system control for the overall radar. All modules are interconnected via coaxial cables with matched lengths and impedance to ensure stable signal transmission. Additionally, the transceiver array adopts a linear array configuration with 2 transmit antennas and 4 receive antennas. The two transmit antennas operate in a TDM mode, ensuring orthogonal transmission and channel separability at the receiver. The experimental platform is deployed in an outdoor environment to validate its performance under realistic conditions.

The practical imaging performance is validated through an outdoor experiment using a DJI AIR 3 unmanned aerial vehicle (UAV) as a target, as shown in Fig. 5. A trihedral metallic corner reflector (7.7 cm × 7.7 cm × 7.7 cm) is mounted on the UAV to provide a stable, high-radar-cross-section (RCS) reference. All subsequent experiments and imaging verifications are performed based on this UAV configuration to ensure consistency in system validation.

Fig. 5. The imaging target of UAV with a metallic corner reflector.

TABLE I
Experimental Parameters Configurations

Parameters	Value
Carrier frequency f_c	10 GHz
Bandwidth B	8 GHz
Pulse width T_w	2 ms
Pulse repetition period T_p	2.5 ms
Number of Tx channel M	2
Number of Rx channel N	4
Tx antenna spacing d_{tx}	60 cm
Rx antenna spacing d_{rx}	15 cm
Tx and Rx antenna spacing d_{tr}	50 cm
Sampling rate f_s	10 MSa/S
Sampling points L	20000
Number of segment P	1000
Minimum scanning angle θ_{min}	-20°
Maximum scanning angle θ_{max}	20°
Scanning angle step $\Delta\theta$	0.2°
Scanning points Q	201

The key experimental parameters are summarized in Table I. As configured, the generated broadband radar signal has a carrier frequency f_c of 10 GHz, a bandwidth B of 8 GHz, a pulse width T_w of 2 ms, and a pulse repetition period T_p of 2.5 ms. The Tx spacing is d_{tx} = 60 cm, the Rx spacing is d_{rx} = 15 cm, and the separation between the last Tx and the first Rx is d_{tr} = 50 cm. This physical configuration yields $M\times N$ = 8 unique transmit-receive pairs, i.e., 8 virtual antenna elements. It is important to emphasize that the equivalent virtual array element spacing is larger than the minimum half-wavelength, calculated as $\lambda_{min}/2 = (c/f_{max})/2 \approx 0.8$ cm $\ll$ 15 cm. Consequently, applying conventional narrowband DBF to this sparse virtual array would result in severe grating lobes, degrading angular resolution and introducing angular estimation ambiguities. The ADC sampling rate f_s is set to 10 MSa/s, resulting in a total of $L = T_w/f_s$ = 20000 sampling points per pulse. For the segmented DBF processing, we segment the data into P = 1000 equal parts, so each segment spans B/P = 8 MHz (i.e., $(B/P)/f_0$ = 0.08%), which is well within the typical ≤ 10% narrowband criterion. For imaging, the DBF scanning range (θ_{min}, θ_{max}) is set to (-20°, 20°), with step $\Delta\theta$ = 0.2°, giving $Q = (\theta_{max}-\theta_{min})/\Delta\theta+1$ = 201 steering directions.

B. Imaging Results Comparison

This section presents a comparative analysis of the 2D imaging performance achieved by three algorithms: conventional DBF, STD-compensated DBF, and the proposed segmented DBF.

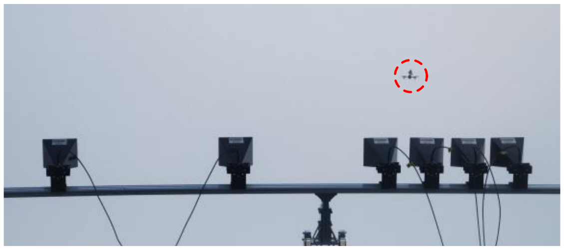

Fig. 6. The experimental detection scenario with a single target located to the right of the boresight.

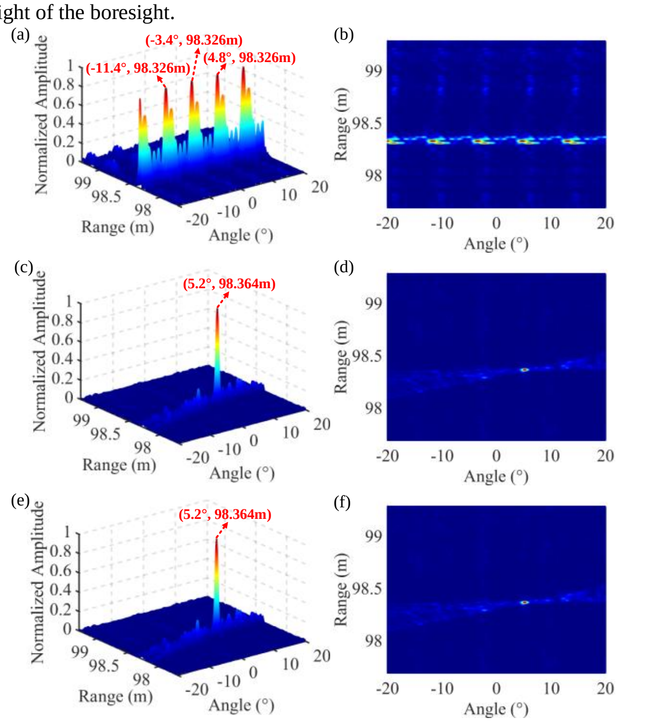

Fig. 7. The imaging results for a target located approximately to the right of the boresight using different algorithms. (a), (c), (e) 3D meshes obtained by the conventional DBF, the STD-compensated DBF, and our segmented DBF algorithm, respectively. (b), (d) and (f) corresponding top view plots.

The experimental scenario, depicted in Fig. 6, involved a single target positioned to the right of the array boresight. The implemented microwave photonic broadband MIMO radar is used to acquire the de-chirped data corresponding to the scene. The de-chirped data are processed using the conventional DBF, the STD-compensated DBF, and the proposed segmented DBF algorithm, respectively. The resulting images are presented in Fig. 7 for direct comparison.

As Fig. 7 (a) reveals, the conventional DBF result exhibits multiple peaks of comparable amplitude at approximately the same range (≈ 98.326 m) but different angles (e.g., -11.4°, -3.4°, 4.8°). These spurious peaks arise from grating lobes inherent to the sparse virtual aperture, which introduce ambiguity in identifying the true target angle. Furthermore, the application of the narrowband assumption to this broadband system introduces beam squint, which manifests as a defocused main lobe and elevated sidelobe levels. In contrast, both the STD-compensated DBF and the segmented DBF algorithms correctly recover a single target at 98.364 m and 5.2°, consistent with the experimental scenario. This result confirms the capability of both compensation algorithms to provide accurate target localization, reliable angular estimation, and an effectively extended unambiguous angular range.

The top-view plots in Fig. 7 (b), (d), and (f) provide a clearer comparison of imaging results. In the conventional DBF result (Fig. 7 (b)), the combined effects of beam squint and grating lobes severely distort the angular spectrum, creating multiple false peaks and smearing the main lobe. In contrast, both the STD-compensated DBF and segmented DBF algorithms produce well-focused main lobe, with clutter and sidelobes significantly suppressed.

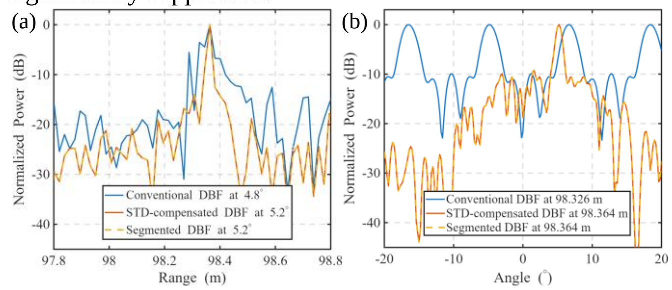

Fig. 8. The profile comparison of the imaging results obtained by different algorithms. (a) Range profiles extracted at the peak angle of each algorithm. (b) Angle profiles extracted at the peak range of each algorithm.

To further compare the background suppression, the range and angle profiles of the three imaging results are shown in Fig. 8. For a fair comparison, the profiles are extracted at the corresponding peak positions of each algorithm, namely 4.8° and 98.326 m for conventional DBF and 5.2° and 98.364 m for both STD-compensated DBF and segmented DBF. As shown in Fig. 8 (a), conventional DBF exhibits stronger fluctuations and a higher background floor in the range profile, while STD-compensated DBF and segmented DBF suppress the background around the target response. In the angle profiles shown in Fig. 8 (b), conventional DBF exhibits pronounced grating lobes and high background fluctuations across the scanning range. In contrast, STD-compensated DBF and segmented DBF suppress the distributed grating-lobe background and concentrate the target response around the correct angle. These results indicate that the proposed segmented DBF effectively corrects beam squint and suppresses grating-lobe artifacts, achieving imaging quality comparable to STD-compensated DBF and markedly improved over conventional DBF.

C. Resolution Analysis

This section quantitatively evaluates the range and angular resolutions of the proposed segmented DBF algorithm. The target is placed around the center of the boresight to avoid beam broadening effects, thereby enabling a clear assessment of the resolution performance (Fig. 9).

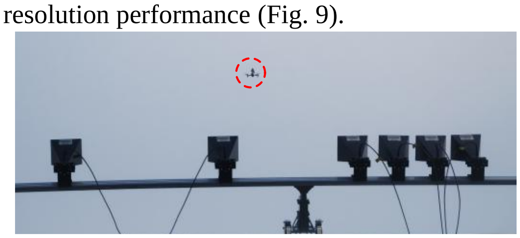

Fig. 9. Experimental detection scenario with a single target located at the center of the boresight.

The imaging results are presented in Fig. 10, where Fig. 10 (a) shows the 3D mesh plot, and Fig. 10 (b) provides the corresponding top-view plot. The target is located at a range of 96.084 m and an angle of -0.8°. According to equation (12), with a signal bandwidth of 8 GHz, the theoretical range resolution is calculated as $\Delta R = c/(2 \times B) = 1.875$ cm. According to equation (13), with $M \times N = 2 \times 4$ virtual elements and spacing $d = 0.15$ m, the virtual aperture is $D = (MN-1)d = 1.05$ m, yielding a theoretical angular resolution of 0.8°.

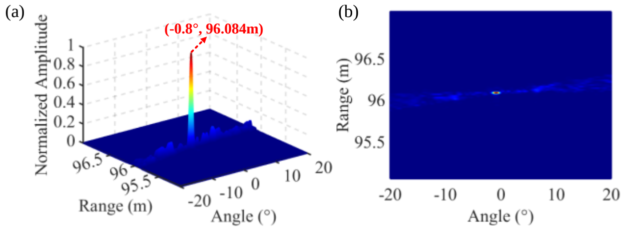

Fig. 10. The imaging results for a target located at the center of the boresight obtained by the segmented DBF algorithm. (a) 3D mesh plot of imaging result. (b) corresponding top-view plot.

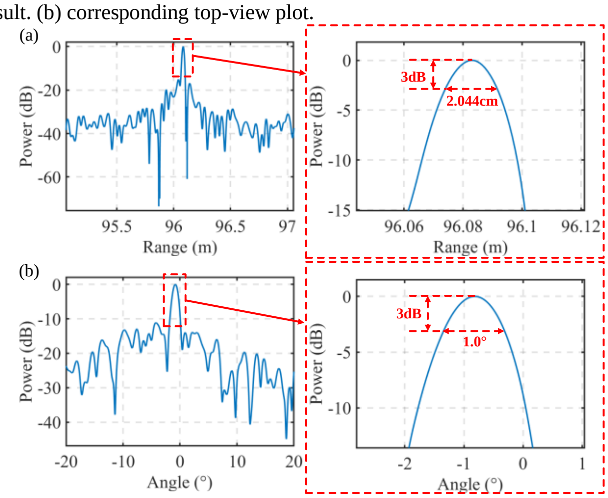

Fig. 11. The range and angle profiles of the imaging results. (a) Range profile at an angle of -0.8°. (b) Angle profile at a range of 96.084 m.

Fig. 11 shows the range and angle profiles of the imaging result. The measured range resolution, defined as the -3 dB width of the range profile in Fig. 11 (a), is 2.044 cm, which is close to the theoretical range resolution of 1.875 cm. Similarly, the measured -3 dB angle width in Fig. 11 (b), is 1.0°, which is close to the theoretical angle resolution 0.8°. The slight discrepancies between the measured and theoretical resolutions are mainly attributed to practical measurement factors, such as the non-ideal point-target response and scattering characteristics of the measured target. These results confirm that segmented DBF delivers centimeter-level range resolution and near-theoretical angular resolution.

D. Multi-target Detection

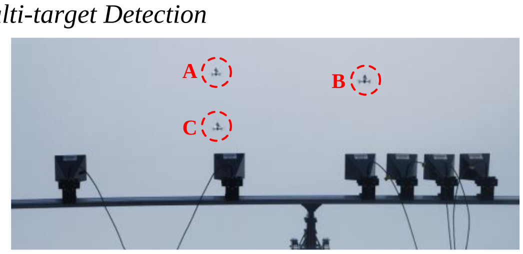

Fig. 12. The experimental detection scenario with multiple targets located at different angles.

To validate the multi-target detection capability of the proposed segmented DBF algorithm, an experiment is configured with three targets placed at different angles. As shown in Fig. 12, targets A and C are located on the left of the boresight, while the other target B is located on the right of the boresight.

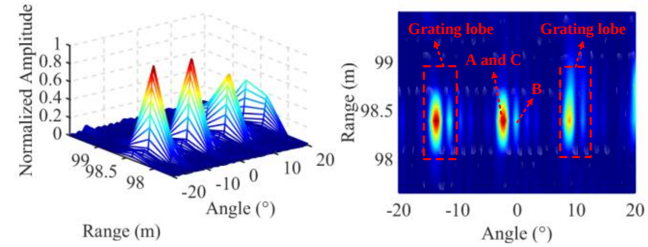

Fig. 13. The imaging results for three targets obtained using the narrowband data. (a) 3D mesh plot of 2D imaging result. (b) Top-view plot of 2D imaging result.

For comparative analysis, an equivalent narrowband data is generated by truncating the time-domain window of the de-chirped signals to 1/20 of the original pulse width. Exploiting the linear-frequency mapping of the de-chirped signal, this truncation limits the signal bandwidth to 400 MHz (spanning 10GHz to 10.4GHz), corresponding to a range resolution of 37.5 cm.

The imaging results obtained from the narrowband data are shown in Fig. 13. The 3D mesh plot in Fig. 13 (a) exhibits multiple peaks, making it difficult to identify the true targets. The top-view in Fig. 13 (b) further shows that targets A and C, which are at similar azimuth angles, merge together and cannot be adequately resolved in range. Moreover, due to insufficient grating lobe suppression inherent to the narrowband configuration, numerous false targets are present in the image.

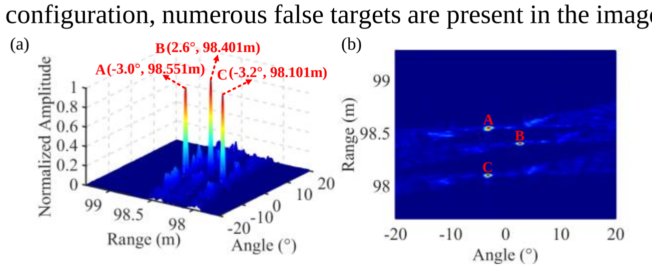

Fig. 14. The imaging results for three targets obtained using the broadband data. (a) 3D mesh plot of 2D imaging result. (b) Top-view plot of 2D imaging result.

In contrast, the imaging results obtained from the broadband data using the segmented DBF algorithm for this multi-target data are shown in Fig. 14. The 3D mesh plot in Fig. 14 (a) clearly shows two distinct responses on the left of boresight at (-3.0°, 98.551 m) and (-3.2°, 98.101 m), corresponding to targets A and C. Although their azimuthal angles differ by only 0.2°, the wideband range resolution allows unambiguous discrimination. A third well-separated response at (2.6°, 98.401 m) corresponds to target B, consistent with the experimental geometry. The top-view in Fig. 14 (b) consistently shows targets A and C on the left and target B on the right, matching the experimental setup. The faint funnel-shaped energy trails are residual, frequency-dependent grating-lobe artifacts whose trajectories vary across sub-bands. The segmented DBF largely decorrelates these lobes, dispersing their energy over range-angle cells and preserving the main-lobe peaks.

This article has been accepted for publication in Journal of Lightwave Technology. This is the author's version which has not been fully edited and content may change prior to final publication. Citation information: DOI 10.1109/JLT.2026.3703868

Overall, the comparison between Fig. 13 and Fig. 14 demonstrates that the broadband microwave photonic MIMO radar offers substantially enhanced capability in resolving clustered targets. The segmented DBF algorithm leverages the broadband characteristics to suppress beam squint and provide accurate multi-target localization in both range and angle.

E. Computational Efficiency Analysis

This section provides a comparative analysis of the computational efficiency of the conventional, STD-compensated, and proposed segmented DBF algorithms. First, the theoretical time complexity of each algorithm is analyzed. The theoretical analysis is then corroborated by measuring the actual signal processing time using the experimental dataset. The complexity analysis uses parameters consistent with the experimental setup described in Section III-A. The time complexity of different imaging algorithms is summarized in Table II.

TABLE II
TIME COMPLEXITY OF DIFFERENT IMAGING ALGORITHMS

Algorithms	Time Complexity
Conventional DBF	$O(L\times MN\times Q+MN\times L\log L)$
STD-compensated DBF	$O(L\times MN\times Q+Q\times MN\times L\log L)$
Segmented DBF	$O(L\times MN\times Q+Q\times L\log L)$

For the conventional algorithm, each of the MN virtual channels undergoes an L-point FFT to form range profiles, resulting in a computational cost of $O(MN\times L\log L)$. Subsequently, DBF is performed across Q steering directions for all L frequency bins, requiring $O(L\times MN\times Q)$ operations. Accordingly, the total time complexity of the conventional algorithm is given by $O(L\times MN\times Q+MN\times L\log L)$.

For the STD-compensated DBF algorithm, beam squint correction is performed by applying a time-domain phase compensation to each sample of every virtual channel for all Q steering directions. This compensation requires $Q\times MN\times L$ operations. After compensation, an L-point FFT is performed for each direction and channel, introducing an additional computational cost of $Q\times MN\times L\log L$. Accordingly, the total time complexity becomes $O(L\times MN\times Q+Q\times MN\times L\log L)$, which is substantially higher than that of the conventional algorithm.

For the proposed segmented DBF algorithm, each de-chirped signal is first divided into P time-domain segments. Within each segment, DBF is performed across Q steering directions using time-domain samples from all MN virtual channels, resulting in a total computational cost of $L\times MN\times Q$. After the segmented DBF, an L-point FFT is applied to each direction to obtain the range profiles, requiring an additional $Q\times L\log L$ operations. Accordingly, the time complexity of the segmented DBF algorithm is given by $O(L\times MN\times Q+Q\times L\log L)$. Since the number of steering directions Q is slightly larger than the number of virtual channels MN in practical systems, the number of additional FFT operations introduced by segmentation is approximately (Q-MN). Therefore, the overall computational complexity of the segmented DBF algorithm remains comparable to the conventional algorithm.

To validate the computational efficiency of the proposed algorithm, experiments are conducted on a computer equipped with an AMD Ryzen 9 7945HX CPU and 2×8GB Samsung DDR5-5600MHz memory. The signal processing time required by different algorithms under identical conditions are shown in Fig. 15. The conventional algorithm completes signal processing in 0.06 s, while the STD-compensated DBF algorithm requires 0.50 s. In contrast, the proposed segmented DBF algorithm completes the signal processing in only 0.07 s. The experimental results demonstrate that the processing speed of the proposed algorithm is approximately 7.1 times faster than that of the STD-compensated DBF algorithm, while maintaining a performance level similar to that of the conventional algorithm.

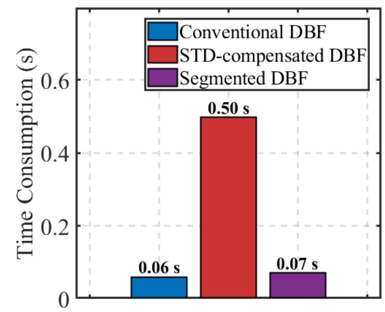

Fig. 15. The actual computation time for different imaging algorithms using experimental data.

Although both the STD-compensated DBF and the segmented DBF algorithm address the beam squint issue in broadband radar systems, the STD-compensated DBF algorithm significantly increases the computational load due to repeated time-domain compensation and FFT operations for each beam direction. The proposed segmented DBF, by leveraging time-domain segmentation and parallel sub-band processing, achieves comparable imaging precision with dramatically higher computational efficiency.

IV. CONCLUSION

This paper has presented the implementation and comprehensive experimental validation of a microwave photonic broadband MIMO array radar system. The system utilizes microwave photonic techniques to generate and process broadband radar signals for high range resolution. Furthermore, it employs a MIMO array architecture to synthesize a large virtual aperture, which provides enhanced angular resolution. To overcome the challenges of beam squint and high computational complexity in such broadband array systems, a novel segmented DBF algorithm was proposed and implemented. Experimental results from a 2×4 photonic MIMO radar with 8 GHz bandwidth demonstrate a range resolution of 2.04 cm and an angular resolution of 1.0°. The proposed algorithm improves imaging speed by a factor of 7.1 compared with STD-compensated DBF algorithm, while effectively correcting beam squint and suppressing grating lobes in both single and multiple UAV detection scenarios. These results collectively verify the system's capability for high-resolution, squint-free, and rapid 2D imaging, showcasing the successful synergy of microwave photonics and advanced digital signal processing for next-generation radar systems. While the present implementation is based on an LFM waveform, extending the proposed approach to other waveform formats, such as stepped frequency and triangular FMCW waveforms, will be investigated in future work.

References

[1] S. Yuan, F. Fioranelli, and A. Yarovoy, "3D high-resolution imaging algorithm using 1D MIMO array for autonomous driving application," *IEEE Trans. Radar Syst.*, vol. 2, pp. 1186–1199, 2024.

[2] B. Li, S. Wang, J. Zhang, X. Cao, and C. Zhao, "Ultra-Fast Accurate AoA Estimation via Automotive Massive-MIMO Radar," *IEEE Trans. Veh. Technol.*, vol. 71, no. 2, pp. 1172–1186, Feb. 2022.

[3] T. Yang, J. Zheng, T. Su, and H. Liu, "Fast and robust super-resolution DOA estimation for UAV swarms," *Signal Process.*, vol. 188, p. 108187, Nov. 2021.

[4] R. D. Palmer *et al.*, "Horus—A Fully Digital Polarimetric Phased Array Radar for Next-Generation Weather Observations," *IEEE Trans. Radar Syst.*, vol. 1, pp. 96–117, 2023.

[5] A. Pirkani *et al.*, "High-Resolution Augmented Multimodal Sensing of Distributed Radar Network," *IEEE Trans. Radar Syst.*, vol. 3, pp. 905–918, 2025.

[6] W. Yi, T. Zhou, Y. Ai, and R. S. Blum, "Suboptimal Low Complexity Joint Multi-Target Detection and Localization for Non-Coherent MIMO Radar With Widely Separated Antennas," *IEEE Trans. Signal Process.*, vol. 68, pp. 901–916, 2020.

[7] J. Yao and J. Capmany, "Microwave photonics," *Sci. China Inf. Sci.*, vol. 65, no. 12, p. 221401, Dec. 2022.

[8] J. Capmany and D. Novak, "Microwave photonics combines two worlds," *Nat. Photonics*, vol. 1, no. 6, pp. 319–330, Jun. 2007.

[9] X. Yu *et al.*, "Broadband stepped-frequency radar waveform generation by Fourier domain mode-locking period-one laser dynamics," *Opt. Lett.*, vol. 49, no. 15, p. 4266, Aug. 2024.

[10] L. Wang *et al.*, "Photonic Generation of Multi-Format Radar Waveforms Based on an Integrated Silicon IQ Modulator," *IEEE J. Sel. Top. Quantum Electron.*, vol. 28, no. 5: Lidars and Photonic Radars, pp. 1–7, Sep. 2022.

[12] F. Zhang, Q. Guo, and S. Pan, "Photonics-based real-time ultra-high-range-resolution radar with broadband signal generation and processing," *Sci. Rep.*, vol. 7, no. 1, p. 13848, Oct. 2017.

[13] F. Zhang *et al.*, "Photonics-based broadband radar for high-resolution and real-time inverse synthetic aperture imaging," *Opt. Express*, vol. 25, no. 14, p. 16274, Jul. 2017.

[14] J. Kong, F. Zhang, Y. Zhou, Y. Wang, H. Wang, and S. Pan, "Advancements of Photonics-based MIMO Radar in High-Resolution Detection of Small Cluster Targets," in *2025 Asia Communications and Photonics Conference (ACP)*, Jiangsu, China: IEEE, Nov. 2025, pp. 1–4. Accessed: May 27, 2026. [Online]. Available: https://ieeexplore.ieee.org/document/11350494/

[15] C. Ma *et al.*, "High-Resolution Microwave Photonic Radar With Sparse Stepped Frequency Chirp Signals," *IEEE Trans. Geosci. Remote Sens.*, vol. 60, pp. 1–10, 2022.

[16] J. Li and P. Stoica, "MIMO Radar with Colocated Antennas," *IEEE Signal Process. Mag.*, vol. 24, no. 5, pp. 106–114, Sep. 2007.

[17] C. Schuessler, M. Hoffmann, and M. Vossiek, "Super-Resolution Radar Imaging with Sparse Arrays Using a Deep Neural Network Trained with Enhanced Virtual Data," *IEEE J. Microw.*, vol. 3, no. 3, pp. 980–993, Jul. 2023.

[18] Z. Peng and C. Li, "A Portable K-Band 3-D MIMO Radar With Nonuniformly Spaced Array for Short-Range Localization," *IEEE Trans. Microw. Theory Tech.*, pp. 1–12, 2018.

[19] G. Serafino *et al.*, "A Photonics-Assisted Multi-Band MIMO Radar Network for the Port of the Future," *IEEE J. Sel. Top. Quantum Electron.*, vol. 27, no. 6, pp. 1–13, Nov. 2021.

[20] B. Wang, M. Jian, F. Gao, G. Y. Li, and H. Lin, "Beam Squint and Channel Estimation for Wideband mmWave Massive MIMO-OFDM Systems," *IEEE Trans. Signal Process.*, vol. 67, no. 23, pp. 5893–5908, Dec. 2019.

[21] S.-H. Park, B. Kim, D. K. Kim, L. Dai, K.-K. Wong, and C.-B. Chae, "Beam Squint in Ultra-Wideband mmWave Systems: RF Lens Array vs. Phase-Shifter-Based Array," *IEEE Wirel. Commun.*, vol. 30, no. 4, pp. 82–89, Aug. 2023.

[22] M. Monemi, M. Rasti, O. Yazdani, O. Lopez, and M. Latva-aho, "Beam Squint Mitigation in Wideband Hybrid Beamformers: Full-TTD, Sparse-TTD, or Non-TTD?," Jun. 25, 2025, *arXiv*: arXiv:2506.19381. Accessed: Nov. 12, 2025. [Online]. Available: http://arxiv.org/abs/2506.19381

[23] B. Paul, K. Sertel, and N. K. Nahar, "Photonic Beamforming for 5G and Beyond: A Review of True Time Delay Devices Enabling Ultra-Wideband Beamforming for mmWave Communications," *IEEE Access*, vol. 10, pp. 75513–75526, 2022.

[24] F. Liu, R. Wu, Z. Du, H. Chen, Z. Tang, and S. Pan, "Wideband Microwave Photonic Beamformer Based on a Spiral Bragg Grating Waveguide," in *2023 International Topical Meeting on Microwave Photonics (MWP)*, Nanjing, China: IEEE, Oct. 2023, pp. 1–4. Accessed: Sep. 20, 2025. [Online]. Available: https://ieeexplore.ieee.org/document/10416605/

[25] V. Dyadyuk, X. Huang, L. Stokes, and J. Pathikulangara, "Implementation of wideband digital beam forming in the E-band," *Int. J. Microw. Wirel. Technol.*, vol. 3, no. 3, pp. 259–266, Jun. 2011.

[26] Tuan Do-Hong and P. Russer, "Signal processing for wideband array applications," *IEEE Microw. Mag.*, vol. 5, no. 1, pp. 57–67, Mar. 2004.

[27] Y. Zhou, F. Zhang, J. Kong, and S. Pan, "High-resolution 3D imaging by microwave photonic time division multiplexing-multiple-input-multiple-output radar with broadband digital beamforming," *IET Radar Sonar Navig.*, vol. 18, no. 9, pp. 1531–1540, Sep. 2024.

[28] Y. Zhou *et al.*, "Field Trial of Cluster Target Detection by Broadband Microwave Photonic MIMO Radar," *IEEE J. Microw.*, vol. 5, no. 3, pp. 631–639, May 2025.

[29] N. H. Lehmann *et al.*, "Evaluation of Transmit Diversity in MIMO-Radar Direction Finding," *IEEE Trans. Signal Process.*, vol. 55, no. 5, pp. 2215–2225, May 2007.

[30] X. Chen, Z. Dong, Z. Zhang, C. Tu, T. Yi, and Z. He, "Very High Resolution Synthetic Aperture Radar Systems and Imaging: A Review," *IEEE J. Sel. Top. Appl. Earth Obs. Remote Sens.*, vol. 17, pp. 7104–7123, 2024.

[31] W.-Q. Wang, "Virtual Antenna Array Analysis for MIMO Synthetic Aperture Radars," *Int. J. Antennas Propag.*, vol. 2012, pp. 1–10, 2012.

[32] I. Podkurkov, J. Zhang, A. F. Nadeev, and M. Haardt, "Efficient Multidimensional Wideband Parameter Estimation for OFDM Based Joint Radar and Communication Systems," *IEEE Access*, vol. 7, pp. 112792–112808, 2019.

[33] P. M. McCormick, S. D. Blunt, and J. G. Metcalf, "Wideband MIMO Frequency-Modulated Emission Design With Space-Frequency Nulling," *IEEE J. Sel. Top. Signal Process.*, vol. 11, no. 2, pp. 363–378, Mar. 2017.